REPORT DOCUMENTATION PAGE

Form Approved
OMB No. 0704-0188

1. REPORT DATE *(DD-MM-YYYY)* 12/14/11	**2. REPORT TYPE** Final Technical Report	**3. DATES COVERED** *(From - To)* 9/15/10-9/14/11

4. TITLE AND SUBTITLE
Closed-Loop Control for High Reynolds Number Turbulent Compressible Jets

5a. CONTRACT NUMBER

5b. GRANT NUMBER
FA9550-10-1-0536

5c. PROGRAM ELEMENT NUMBER

6. AUTHOR(S)
Glauser, Mark N. and Lewalle, Jacques

5d. PROJECT NUMBER

5e. TASK NUMBER

5f. WORK UNIT NUMBER

7. PERFORMING ORGANIZATION NAME(S) AND ADDRESS(ES)
Syracuse University
Controllers Office Skytop
Office Bldg, Syracuse, NY 13244-0001

8. PERFORMING ORGANIZATION REPORT NUMBER

9. SPONSORING/MONITORING AGENCY NAME(S) AND ADDRESS(ES)
USAF, AFRL DUNS 143574726
Air Force Office of Scientific Research
875 N. Randolph St. Room 3112
Arlington, VA 22203
Daniel Smith, Grants Officer, Dr. Doug Smith, Program Manager

10. SPONSOR/MONITOR'S ACRONYM(S)
AFOSR

11. SPONSOR/MONITOR'S REPORT NUMBER(S)
AFRL-OSR-VA-TR-2012-0803

12. DISTRIBUTION/AVAILABILITY STATEMENT
Distribution code A

13. SUPPLEMENTARY NOTES

14. ABSTRACT

From the viewpoint of the PIs, this project has been very successful on several fronts. The data acquisition has yielded good acoustic and PIV records; some effect of jet actuators on far-field noise have been measured through spectra and cross-correlations; POD decomposition of near-field velocity shows that cross-correlations with the far-field noise is accounted for by velocity mode 6 within a particular downstream r-θ plane window; the wavelet processing of near-field pressure provides insight into convected flows structures and their possible breakdown, and associates them with distinctive cross-correlations with the far-field; wavelet processing of coherent far-field noise identified individual sources and some of their properties, including precise lags in arrival time at far-field microphones; the calculation of acoustic path refraction by the mean flow yields a table of source locations and far-field lags, which connects for the first time the far-field measurements of individual sources to their approximation locations and properties.

15. SUBJECT TERMS

16. SECURITY CLASSIFICATION OF:			**17. LIMITATION OF ABSTRACT**	**18. NUMBER OF PAGES**	**19a. NAME OF RESPONSIBLE PERSON**
a. REPORT	**b. ABSTRACT**	**c. THIS PAGE**			Mark Glauser
UNCLAS	UNCLAS	UNCLAS	UU		**19b. TELEPHONE NUMBER** *(Include area code)* 315 443 2823

Reset

Final report AFOSR project FA9550-10-1-0536
“Closed-loop Control for High Reynolds Number Turbulent Compressible Jets”

Program Manager: Dr. Doug Smith
9/15/10 – 9/14/11

PI: Mark Glauser, Co-PI: Jacques Lewalle
Department of Mechanical and Aerospace Engineering
Syracuse University
Syracuse, New York 13244-1240
mglauser@syr.edu

I. Executive summary

From the viewpoint of the PIs, this project has been very successful on several fronts. The data acquisition has yielded good acoustic and PIV records; some effect of jet actuators on far-field noise have been measured through spectra and cross-correlations; POD decomposition of near-field velocity shows that cross-correlations with the far-field noise is accounted for by velocity mode 6 within a particular downstream r-θ plane window; the wavelet processing of near-field pressure provides insight into convected flows structures and their possible breakdown, and associates them with distinctive cross-correlations with the far-field; wavelet processing of coherent far-field noise identified individual sources and some of their properties, including precise lags in arrival time at far-field microphones; the calculation of acoustic path refraction by the mean flow yields a table of source locations and far-field lags, which connects for the first time the far-field measurements of individual sources to their approximation locations and properties.

Therefore, the combination of data acquisition, processing by multiple methods and modeling of sound propagation has yielded new insights in the underlying physics. This new understanding opens the possibility of innovative control strategies for the jet noise problem. From the results, the highlights are:

- the observation that velocity POD mode 6, extracted from 10 kHz TRPIV data, carries most of the cross-correlation with the far-field signals;
- the identification and characterization of individual sources from the wavelet transforms of far-field acoustic signals from 3 microphones; and
- the approximate localization of these sources by triangulation, taking the refraction of acoustic paths by the jet’s mean velocity field, is validated by prior knowledge that the most active noise-producing regions are near the collapse of the potential core.

First we list the publications and conference presentations resulting from the work on this grant. Then the body of the report provides a summary of techniques and results in relation to the Statement of Work.

II. List of presentations and publications where credit is given to this grant

Conference Proceedings:

1. "Correlations and wavelet based analysis of near-field and far-field pressure of a controlled high-speed jet", K.R. Low, Z.P. Berger, J. Lewalle, B. El-Hadidi and M.N. Glauser, AIAA paper 1024804, 2011 Hawaii Summer Conferences
2. "Correlations of near- and far-field acoustic data in a high- speed jet", J. Lewalle, K.R. Low, M.N. Glauser and Z.P. Berger, paper # 293144, International Symposium on Turbulent Shear Flow Phenomena, Ottawa, ONT, July 28-31, 2011.

Conference Abstracts:

1. "Modeling unsteady sound refraction by coherent structures in a high-speed jet", P. Kan and J. Lewalle, paper M18.04, Bull. Am. Phys. Soc. 56(18), 2011
2. "Noise source characterization from far-field data in high-speed jets", J. Lewalle, K.R. Low and M.N. Glauser, paper M18.05, Bull. Am. Phys. Soc. 56(18), 2011
3. "Active control of jet noise using high-resolution TRPIV Part 1: POD analysis", Z. Berger, S. Koska, K. Low, M. Berry and M. Glauser, paper M23.06, Bull. Am. Phys. Soc. 56(18), 2011
4. "Active control of jet noise using high-resolution TRPIV Part 2: Velocity-pressure-acoustic correlations", K. Low, S. Koska, Z. Berger, M. Berry, S. Gogineni and M. Glauser, Paper M23.07, Bull. Am. Phys. Soc. 56(18), 2011

Journal Papers being prepared for submission (winter 2011 - 2012):

1. "Investigation of Different Active Flow Control Strategies for High Speed Jets Using Synthetic Jet Actuators", K. R. Low, B. E. Hadidi, M. N. Glauser, to be submitted to AIAA Journal
2. "Correlations and wavelet based analysis of near-field and far-field pressure of a controlled high-speed jet", K.R. Low, Z.P. Berger, J. Lewalle, B. El-Hadidi and M.N. Glauser, to be submitted to AIAA Journal
3. "Properties of jet noise sources from far-field pressure data", J. Lewalle, K.R. Low and M.N. Glauser, to be submitted, Journal of Aeroacoustics.
4. "Sound propagation and refraction in high-speed jets", J. Lewalle and P. Kan, to be submitted, Journal of Aeroacoustics.

III. Statement of Work

The Statement of Work included a timeline with the following highlights

1. Acoustic data acquisition without and with control
2. Identification of near-field spatial structures
3. Correlation of these structures with far-field acoustic measurements
4. Simultaneous PIV/acoustic data acquisition

5. POD decomposition of near-field velocity
6. Combination of correlations, POD, wavelet and other techniques to gain insight in flow physics and relation to far-field noise
7. Use this information toward an evolving strategy for jet noise control

The successive results below cover all items in this list.

IV. Experimental Setup

All experimentation was carried out in the large scale (206 m^3) anechoic jet facility at Syracuse University, Figure 1. Since its construction in the 1970's, under the direction of Dosanjh *et al.*, the anechoic chamber has undergone major upgrades (Tinney *et al.*). The walls are constructed from 1ft thick single-pour concrete. All of the interior walls, floor and ceiling are acoustically treated with fiber glass wedges, with a 150*Hz* cut-off frequency. Housed within the chamber is a jet rig fitted with a matched 5th order polynomial axisymmetric nozzle with an exit diameter of 50.8 mm.

Figure 1: The anechoic chamber at Syracuse University

A. Data acquisition: Hydrodynamic and Acoustic

Near-Field Pressure: The near-field hydrodynamic pressure is acquired model XCE-093-5G, 0-0.34 Bar Kulite pressure transducers. The diameter of the transducers is 2.4*mm*, which allows for a minimal intrusion into the partially hydrodynamic region of measurement. The Kulites require a 10 volt DC excitation which is provided by five 3-channel Endevco model 136 DC differential-voltage amplifiers. The near-field pressure ring was oriented in such a way that captured the fluctuating pressure at two different stream-wise locations in a simultaneous fashion. The two azimuthal arrays of transducers contained 5 Kulites each with one array located at 3 diameters downstream from the jet exit and the other at 6 diameters.

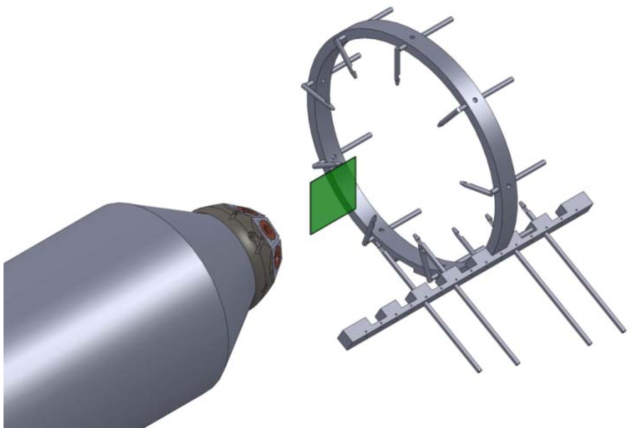

Figure 2: Schematic of the nozzle, kulites and PIV laser sheet in the near field

Far-Field Sound: For far-field sensing 6 - G.R.A.S. type 40BE 1/4 inch pre-polarized free field condenser microphones are arranged in a boom array starting with microphone 6 located 15o from the jet axis with increments of 15o between each microphone, Figure 3. The array is located 75 diameters downstream from the center of the jet exit plane, and is oriented in plane vertically with the jet rig. Excitation is provided by G.R.A.S. type 26CB 1/4 inch preamplifiers. The frequency response and dynamic range of the microphones are 10Hz-40 kHz (+/- 1dB), or 4Hz to 100 kHz (+/- 2dB).

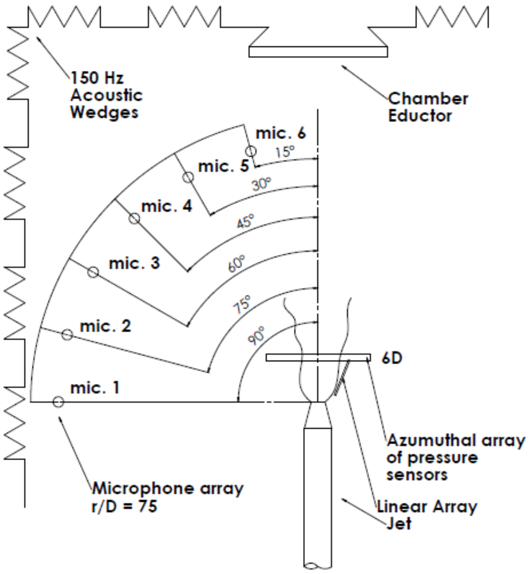

Figure 3: Schematic of the far-field microphones in relation to the jet nozzle

B. Data acquisition, PIV

The work done in conjunction with Spectral Energies (SE) called for the integration of their 2 component TR-PIV system into the experimental setup. The PIV data was sampled simultaneously with the pressure and acoustic data. The system includes a Quantronix Hawk-

Duo Series high energy diode pumped Nd: Yag Laser and a Photron FASTCAM CCD camera. The laser outputs 12mj total energy at 10*kHz*. Both the laser sheet and camera system were mounted in a single traverse in order to have the capability to move the measurement location without the need to recalibrate the system each time. The laser system is considerably larger than the standard PIV systems previously used in the lab so different approaches had to be taken in order to set up the experiment. The chiller and power supply attached to the laser through a series of cables and umbilical cords had to be housed outside the anechoic chamber due to the size (19 x 20 x 28 inches), weight (204lbs), and noise emitted from the system. The cables were routed through a small access hold on the wall behind the jet rig. The limited length of the cabling only allowed us to mound the laser head on a stand adjacent to the jet rig, on the right side (facing the flow). The laser head was oriented such that the beam shot parallel to the jet flow. After this point the beam had to be deflected through a series of turns in order to achieve the laser sheet seen in Figure 4. In the experiments discussed here the beam was shot through a series of 5 turns. The traversing system was then mounted on the left side of the jet (facing the flow), where the camera was mounted, see Figure 4. The laser beam was cantilevered off of the traversing system so that we could shoot the sheet through the centerline of the jet. The reason for having everything mounted on the left side of the jet was to reduce the amount of reflection related noise captured by the far-field microphones, which were located on the right side of the jet rig. Note that when the laser sheet was being traversed back and forth for different measurement locations, the azimuthal and linear pressure array was stationary throughout all cases.

Seeding: In order to seed the bulk flow of the jet, a PIVTEC twelve Laskin nozzle seeding unit was used, in order to withstand the back pressure of the injection into the jet piping (around 10bar). This seeding device uses olive oil as the medium and aerosolizes the particles directly into the bulk flow of the jet. The device produces particles on the order of 1 μm. The pressure of the main seeder was adjusted accordingly with the Mach number of the jet. Pressure of 13, 20, and 25 psi were used for Mach 0.6, 0.85, 1.0, respectively. For the co-flow seeding, a commercial Show Fogger was used in order to provide a uniform distribution of particles throughout the entrainment and bulk flow regions of the jet. The amount of co-flow seeding was also adjusted based on the Mach number of the jet.

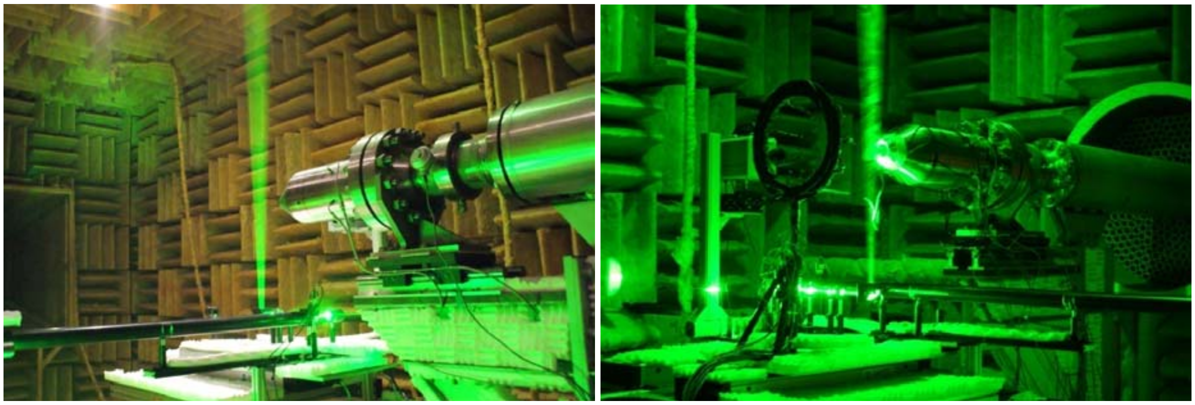

Figure 4: Time Resolved PIV system

C. Actuation Module

The control mechanism used was our third iteration on a family of synthetic jet actuator nozzles redesigned for optimal performance during experimentation. The integrated nozzle consists of a circular array of 8 synthetic jet actuators (zero net-mass-flux). We are able to achieve exit velocities on the order of 50-80 m/s. These actuators are integrated directly into the nozzle of the jet and this design can be seen in Figure 5. The velocities produced by the actuators are sufficient to disturb the developing shear layer. Eight individual slots are located 0.6 mm from the lip of the jet and cover the entire circumference of the nozzle exit to provide actuation uniformly around the out-coming shear layer. The synthetic jets have been designed such that each actuator can be controlled independently to provide actuation patterns in the form of modes 0,1,2, and 4. In addition, the synthetic jets are designed to be inclined towards the jet, at an angle of 45^o. For the cases shown, the forcing in the control is a mode 0 axisymmetric forcing where all synthetic jet actuators are pulsing in phase with the same exit velocities. Due to the way the piezoelectric discs are secured into the cavities of the glove itself, and the variability of the properties from one diaphragm to another, the task of ensuring a uniform velocity out of each individual jet is non-trivial. Therefore much time and effort was spent in making sure a truly axisymmetric forcing was achieved in each case. The schematic of the glove shown below is the third generation glove design used in the current experiments.

Figure 5: Drawings and in-situ photographs of nozzle with actuators

All near-field and far-field sensors are initially sampled at 40.96kHz and low-pass filtered at 20.48kHz via a National Instruments PXI system equipped with three 8-channel NI-4472 A/D converting boards with 24 bits resolution and 8 dedicated low-pass filters. All velocity data are sampled at 10kHz, therefore when performing velocity-pressure and velocity-acoustic correlations all pressure and acoustic data was subsequently resampled at 10kHz and phase aligned with the velocity data. For the raw spectra and correlations shown in section 5.1, all quantities were computed using 46 ensembles of 8192 samples, giving a frequency resolution of fs./ns = 5Hz. For the lowest flow speed (Mach 0.6), the current block length accounts for approximately 800 integral scales, so the sample size could be reduced to increase the number of ensembles if necessary. The phase aligned data was broken up into 8 ensembles of 1024 samples.

V. Results

A. Near-Field and Far-Field Auto Spectra. Figures 6 and 7 show the baseline (a) and open loop (b) near field spectra for both the azimuthal array and the linear array. Good symmetry is seen for the azimuthal plane, which is a characteristic of the jets axisymmetric nature. The linear array shows the decay in the dominant frequencies characteristic to the flow with downstream progression. The relative magnitude of the spectral content in the near-field gradually decreases between 4D and 6D. After this point (after the potential core collapse (average sense)), the curves appear to flatten out and become more broadband. Moreover, as the jet propagates downstream the dominant frequencies in the flow decreases from approximately *900Hz* at *x/D = 4* to *300Hz* at *x/D = 8*. This is associated with the breakdown of the potential core. Review of the controlled vs. baseline spectra doesn't reveal much discernible differences. This could be due to the fact that the actuators are only being driven at 1000Hz. What can be seen is a slight increase in the magnitude of the spectra at 6D, and a collapse of the spectra at 5D as compared to the baseline case.

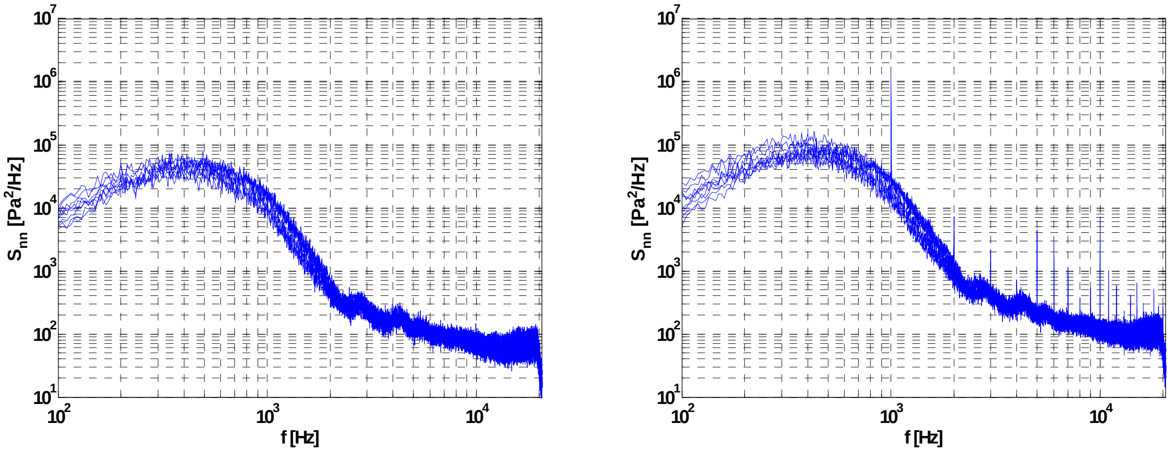

(a) (b)

Figure 6: Near-Field Auto-Spectra for azimuthal array at x/D = 6, (a) baseline and (b) open-loop control

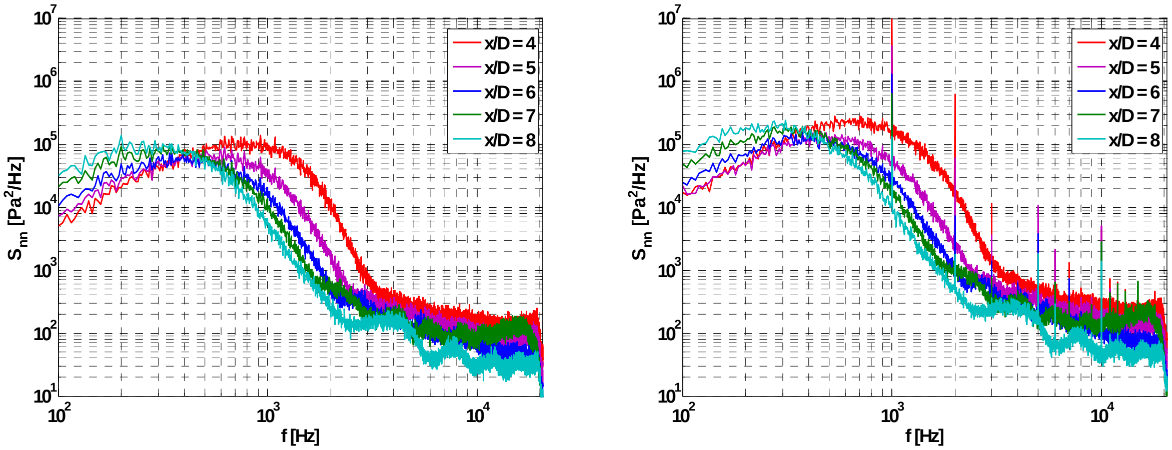

(a) (b)

Figure 7: Near-Field Auto-Spectra for linear array at x/D = 4 - 6, (a) baseline and (b) open-loop control

Figure 8 shows the far field power spectra (dB(A)) for all 6 microphones. All acoustic data acquired is run through an A-weighting filter before computing spectra and correlations. The filter response as defined in ANSI Standards S1.4-1983 and S1.42-2001 is:

$$Ra(f) = \frac{12200^2 * f^4}{(f^2 + 20.6^2)\sqrt{(f^2 + 107.7^2)(f^2 + 737.9^2)}(f^2 + 12200^2)} \tag{8}$$

Consistant with past studies in our group, the power spectra changes from more broadband and lower in magnitude to more narrowband and higher in magnitude as the polar angle shifts from *90^o to 15^o*. This, again has been demonstrated previously and proves the directional nature of the jet. The far-field spectra for the controlled jet effectively pick up the forcing frequency of the actuation. This is a common result of using any actuator for noise reduction purposes, that one hopes will drop out when the test is scaled up to actual dimensions.

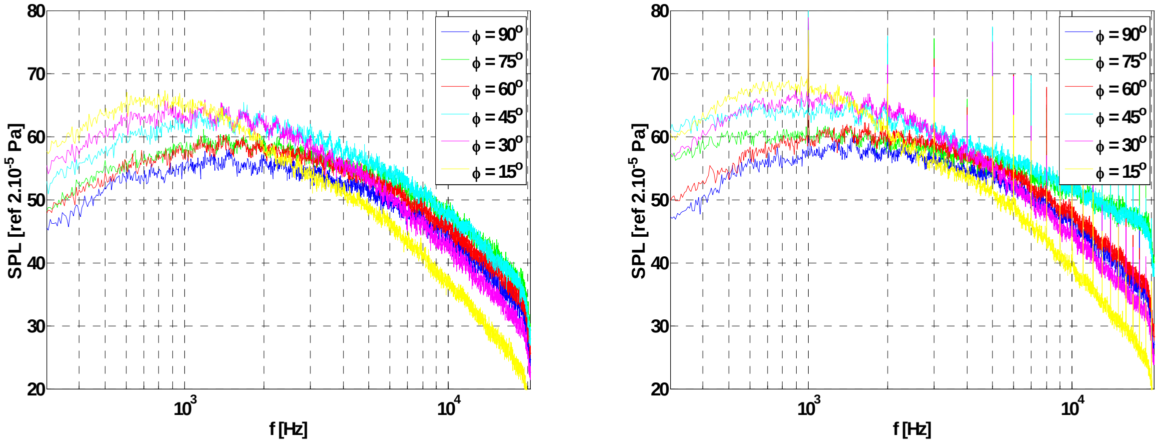

(a) (b)

Figure 8: Far-Field Auto-Spectra in dB(A), (a) baseline and (b) open-loop control

B. The normalized autocorrelations. The autocorrelation represents the time scale of the footprint of structures at different locations both in the near and far-field. In Figure 9 we see the comparison between the autocorrelation function for all 9 Kulites in the azimuthal array for the baseline and controlled jet. The excitation has no effect on the overall time integral scale, but the sinusoidal input of the actuation introduces some periodicity in the correlation. The integral time scale here is approximately 0.5ms. The autocorrelation function is also evaluated for the linear array, Figure 10. The correlation function gradually becomes broader with downstream progression due to the increasing time scale of the passing structures as they propagate downstream. The excited flow autocorrelation functions show the sensors closer to the jet exit are picking up the sinusoidal input response of the actuators. The presence of the sinusoidal oscillations is gradually damped out and appears to be non-existent further downstream.

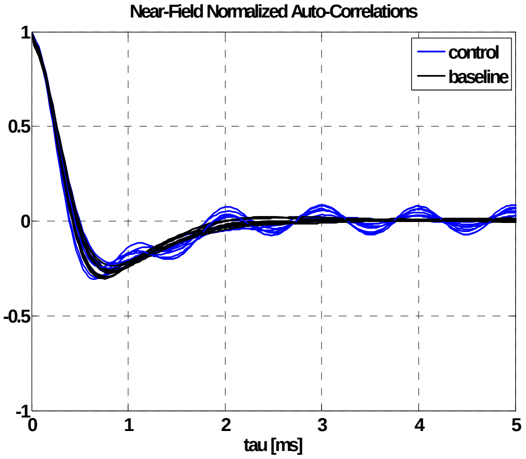

Figure 9: Autocorrelation function for all azimuthal sensors at 6D, (black) baseline and (blue) control

when we reach 8 diameters. It is also known that the presence of large scale structures leads to deeper negative peaks [6]. What is being captured with these plots is the gradual breakup of these strictures downstream as well.

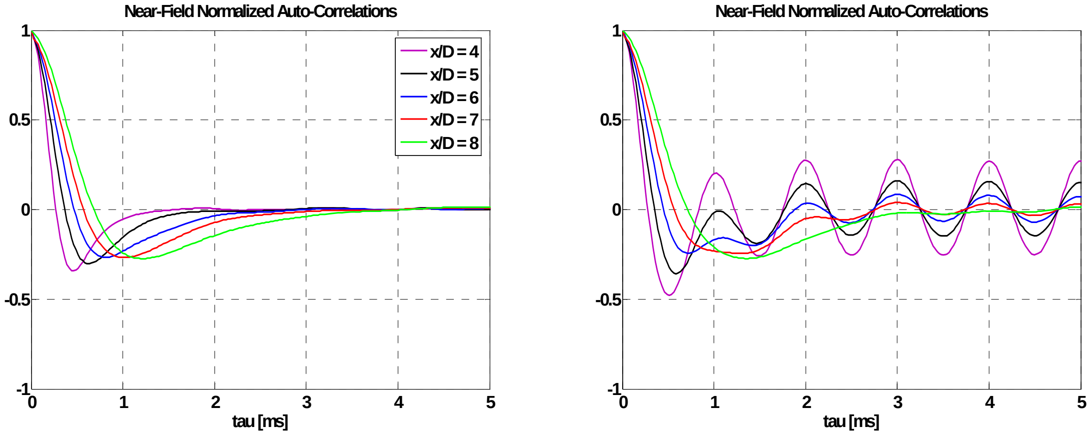

(a) (b)

Figure 10: Autocorrelation functions for the linear array, (a) baseline and (b) control

C. The normalized cross-correlations. Cross-Correlations give insight into the relationship between two different signals. Figure 11 shows the cross correlation for the sensor at 4D and each subsequent sensor in the linear array. From this, one can infer the convective velocity of the jet. As expected, the correlation is strongest with the sensors closest together, with a Gaussian like decay as the sensor gap increases. One important measure by which the propagation of sources to the far-field is evaluated is through that of the near-field to far-field cross correlations. Figures 12 - 14 cover the range of cross-correlations between different near-field quantities and the far-field microphone located at 15 degrees with respect to the jets axis (See Figure 3). The cross-correlation between the linear array of sensors in the near-field shows a correlation delay time window of 9 to 10*ms*, with delay time increasing further away from microphone, Figure 12. The correlation levels for the sensors at 6, 7 and 8D have relatively the same correlation magnitude, whereas 4 and 5D are considerably lower. This is also indicative of the different source properties relative to different regions of the jet (pre and post potential core collapse). Figure 12b shows a reduction in the delay time at 6, 7 and 8D, no change at 5D, and a significant increase in the delay time at 4D when the control is on.

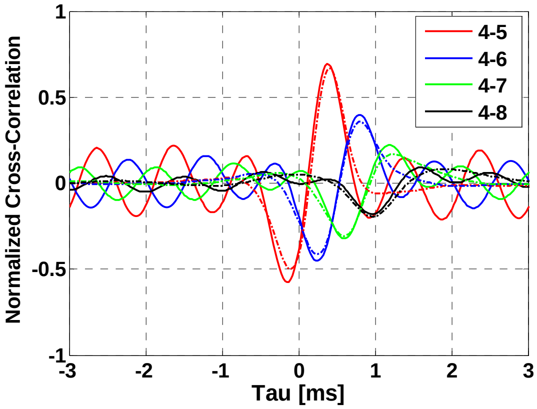

Figure 11: Cross-correlation functions for the linear array, (—) baseline and (···) control

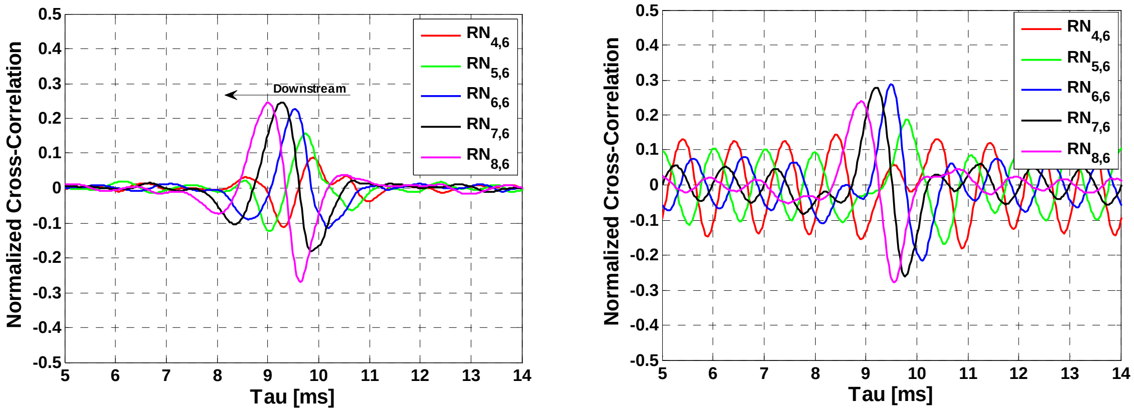

(a)

(b)

Figure 12: Cross-correlation functions for the linear array and the far-field microphone at 15 degrees, (a) baseline and (b) control

Figures 13-14 give some idea of the correlation strength between the sensors in the azimuthal plane at 6D and the far-field. Figure 13 shows the comparison between the baseline and controlled case. The delay time is approximately 9.5ms for the baseline and slightly lower for the controlled jet. The flow field excitation is speeding up the travel time of the sources in the hydrodynamic region. Figure 14 shows the cross-correlation between the Fourier azimuthal mode filtered pressure and the 15 degree microphone. As already demonstrated and analyzed by previous investigators, the correlation between mode 0 and the far-field is the strongest by comparison to the unfiltered pressure and the higher order modes. There is essentially no correlation between mode 1 and the far-field. The control proves to greatly increase the cross-correlation functions, especially for that of mode 0. Mode 1 is polluted with the input signal response due to the actuation.

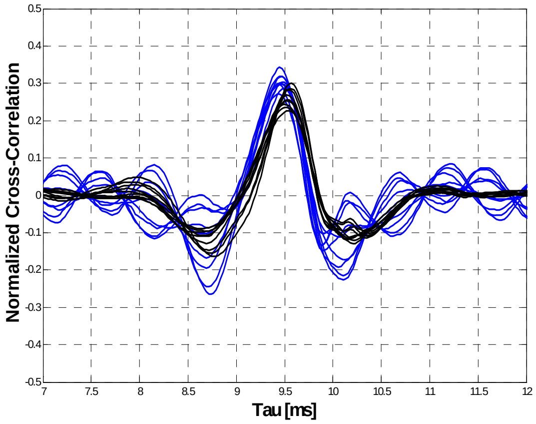

Figure 13: Cross-correlation functions for the azimuthal array of sensors and the far-field microphone at 15 degrees, (black) baseline and (blue) control

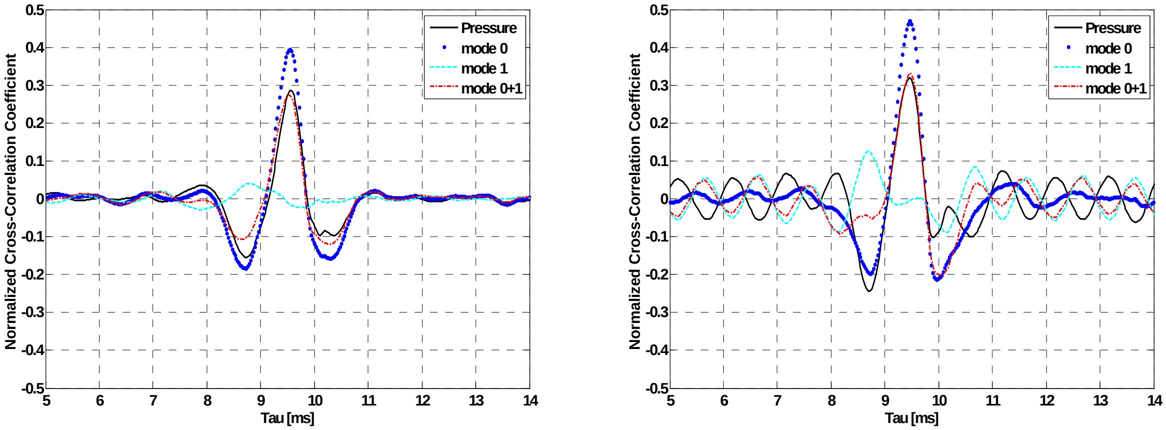

(a) (b)

Figure 14: Cross-correlation functions for the Fourier Filtered modes and the far-field microphone at 15 degrees, (a) baseline and (b) control

D. POD analysis and correlations. Proper Orthogonal Decomposition(POD) was used to resolve the low dimensional characteristics buried within the TR-PIV dataset. We probe the flow-field for the most energetic or coherent structures. POD exploits the rich spectral distinction between large scale coherent motion and the finer scale content. Method of Snapshots was used for this particular study. The integral eigenvalue problem is in equation 9.

$$\int C(t,t')a_n(t')dt' = \lambda^{(n)} a_n(t) \tag{9}$$

Where λ is the eigenvalue, *a*$_n$*(t)* is the temporal eigenfunction, and C(t, t') is the velocity correlation, given in equation 10.

$$C(t,t') = \frac{1}{T}\int u_i(\vec{x},t)u_i(\vec{x},t')d\vec{x} \tag{10}$$

To ensure the correct scaling of the POD modes equation 11, shows the temporal modes should be orthogonal and have a magnitude of the square root of the eigenvalues

$$< a_n \cdot a_m >= \delta_{mn}\lambda^{(n)} \tag{11}$$

The spatial eigenfunction can be calculated from the temporal eigenfunctions using equation 12.

$$\phi^{(n)}(x) = \frac{1}{T\lambda^{(n)}}\int a_n(t)u_i(x,t)dt \tag{12}$$

With the temporal and spatial components of the flow known, the flow can be reconstructed using equation 13.

$$u_i(x,t) = \sum_{n=1}^{N_m} a_n(t)\phi_i^{(n)}(x) \tag{13}$$

For every test case 8623 realizations were acquired at a rate of 10kHz, translating to a total acquisition time of 0.8623s. During processing, all 8623 modes were calculated. As stated above, the limitation of having only one camera facilitated the r-z measurement plane orientation, as opposed to the more typical r-θ plane orientation rigorously studied in our group.

POD Eigenfunctions: Examination of the eigenfunctions bears a direct correlation to the most dominant structures in the flow. Figure 15, (a) – (f) show the first 16 spatial modes $\phi_u^{(n)}$ of the POD for both the baseline (a, c, e) and controlled case (b, d, f), at the three different measurement planes. The spatial eigenfunctions seem to organize themselves in alternating pairs,1 and 2, 3 and 4, 5 and 6, and so on. This trend was implicated by the auto-spectral density plots shown previously. The control seems to break up this trend in all three measurement locations. There is this prominence of very rich physical structure modification caused by this relatively low energy perturbation. This is something that will be further investigated in the future.

POD velocity field reconstructions: Here we show how the POD reconstruction for the first 20 modes (only 0.23% of the total modes to extract 40% of the total energy) at t = 100 compares to the original instantaneous fluctuating velocity field at t = 100. The first three pairs of figures cover the baseline results and the last three pairs represent the controlled results. Examination of the instantaneous snapshots reveals the rich high dimensional nature of the flow. What the reconstructions illustrate is the ability to extract the main features embedded within each realization with only a few modes. This leads to a powerful way to evaluate how the actuation affects the stream-wise components of the velocity field. The reconstruction of the baseline data is able to effectively capture the large scale vorticity generated by the interaction between the exhausted jet plume and the surrounding ambient fluid. The reconstruction of the controlled jet data tells a very different story. We see the emergence of these very distinct pairs of structures seemingly generated by the actuation. These structure pairs seem almost identical and appear to retain their energy as they convect downstream. It is also apparent from Figures 16e and 16f that the control seems to be shortening the potential core length. This is a characteristic of the control that has been indicated in the pressure spectra before, but is now visible here. Note that the

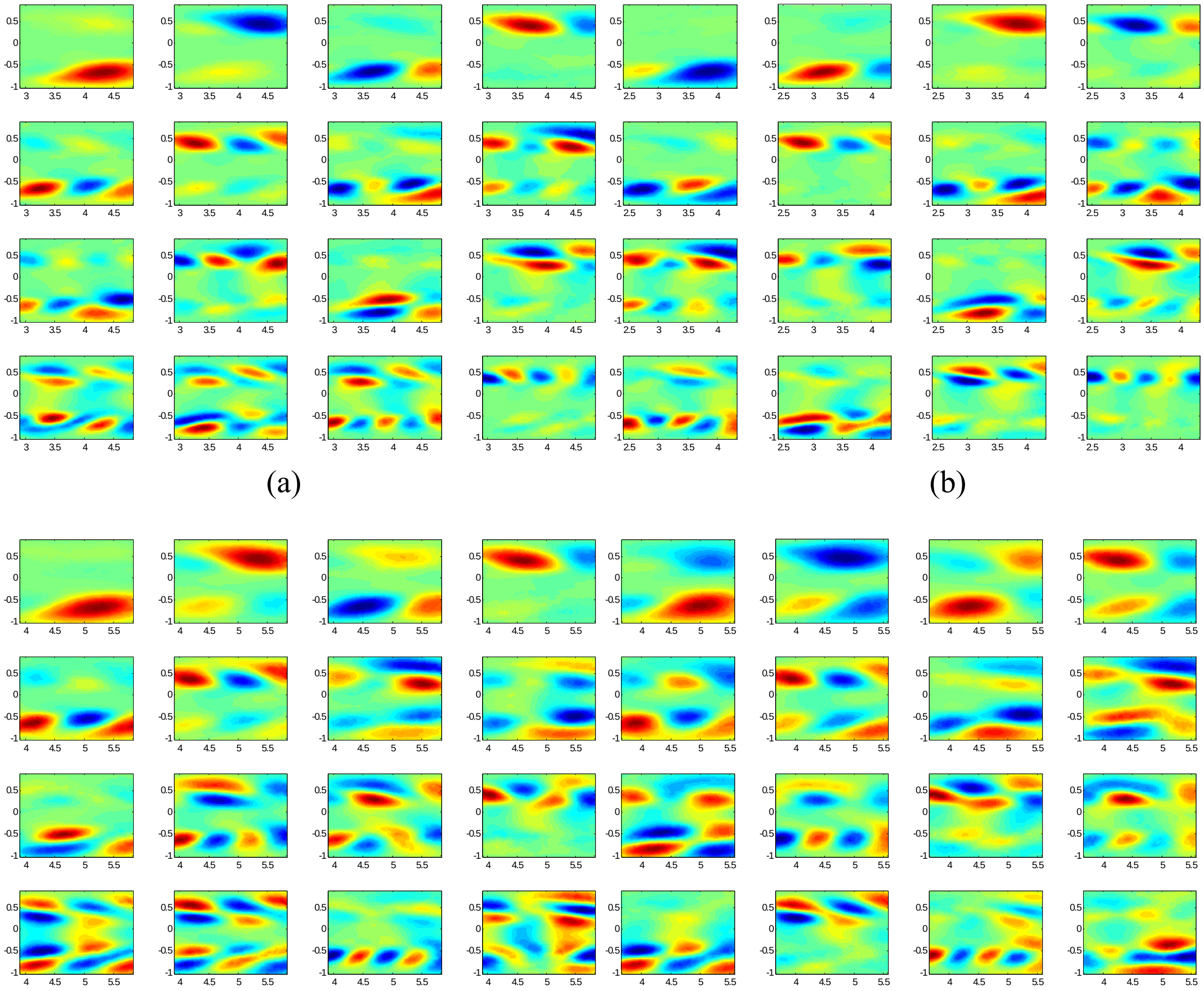

(a) (b)

(c) (d)

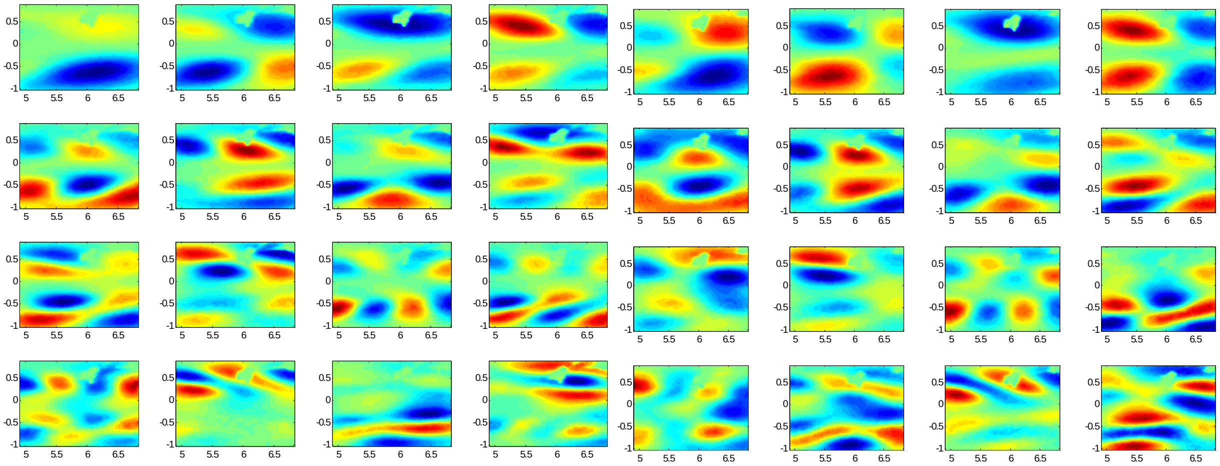

(e) (f)

Figure 15: POD spatial eigenfunctions: (a, c, e) baseline flow, (b, d, f) controlled flow

sections circled in red are where one of the near-field pressure sensors was in the image field of view. This was an unavoidable occurrence due to the configuration of the sensor array.

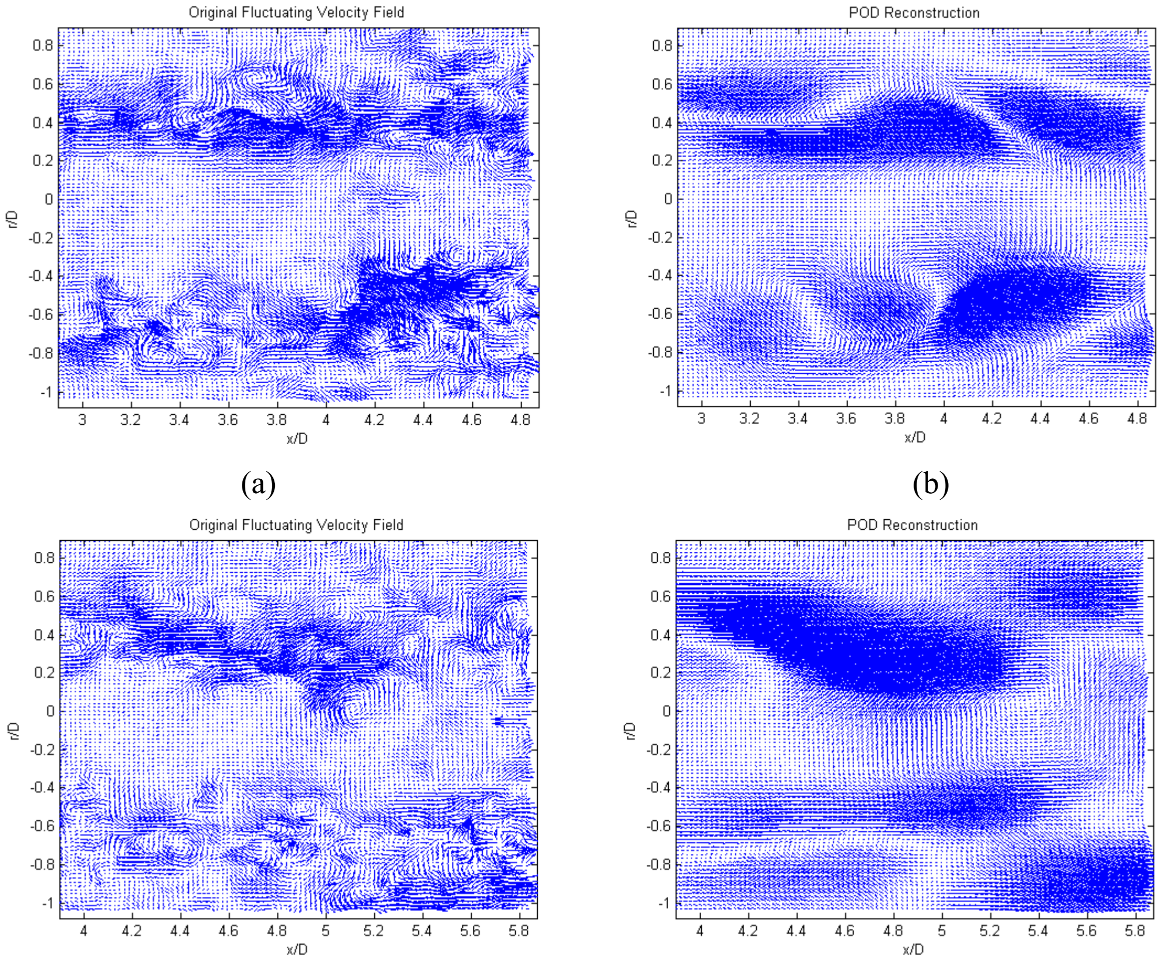

(a) (b)

(c) (d)

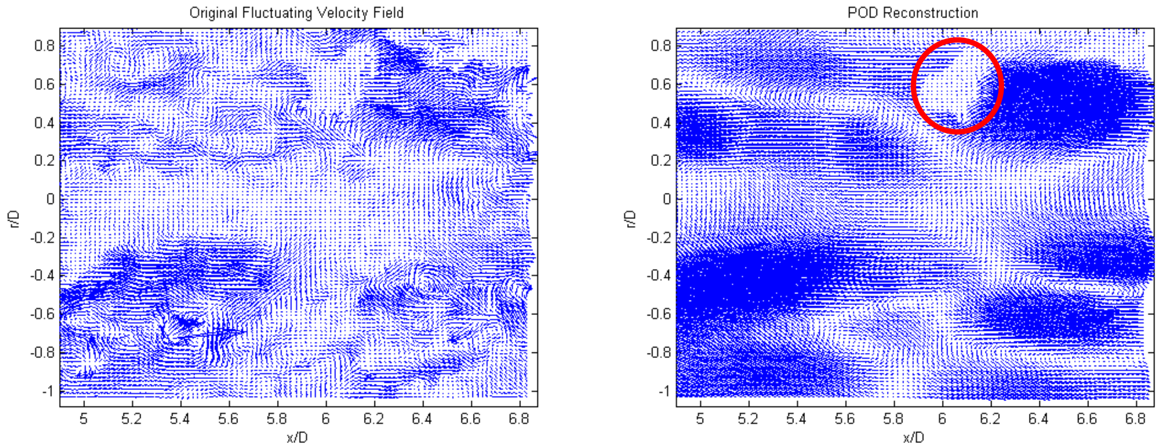

(e) (f)

Figure 16: Stream-wise fluctuating velocity components of the original instantaneous velocity field (left), and the 20 mode reconstruction at three stream-wise locations (right), Baseline flow

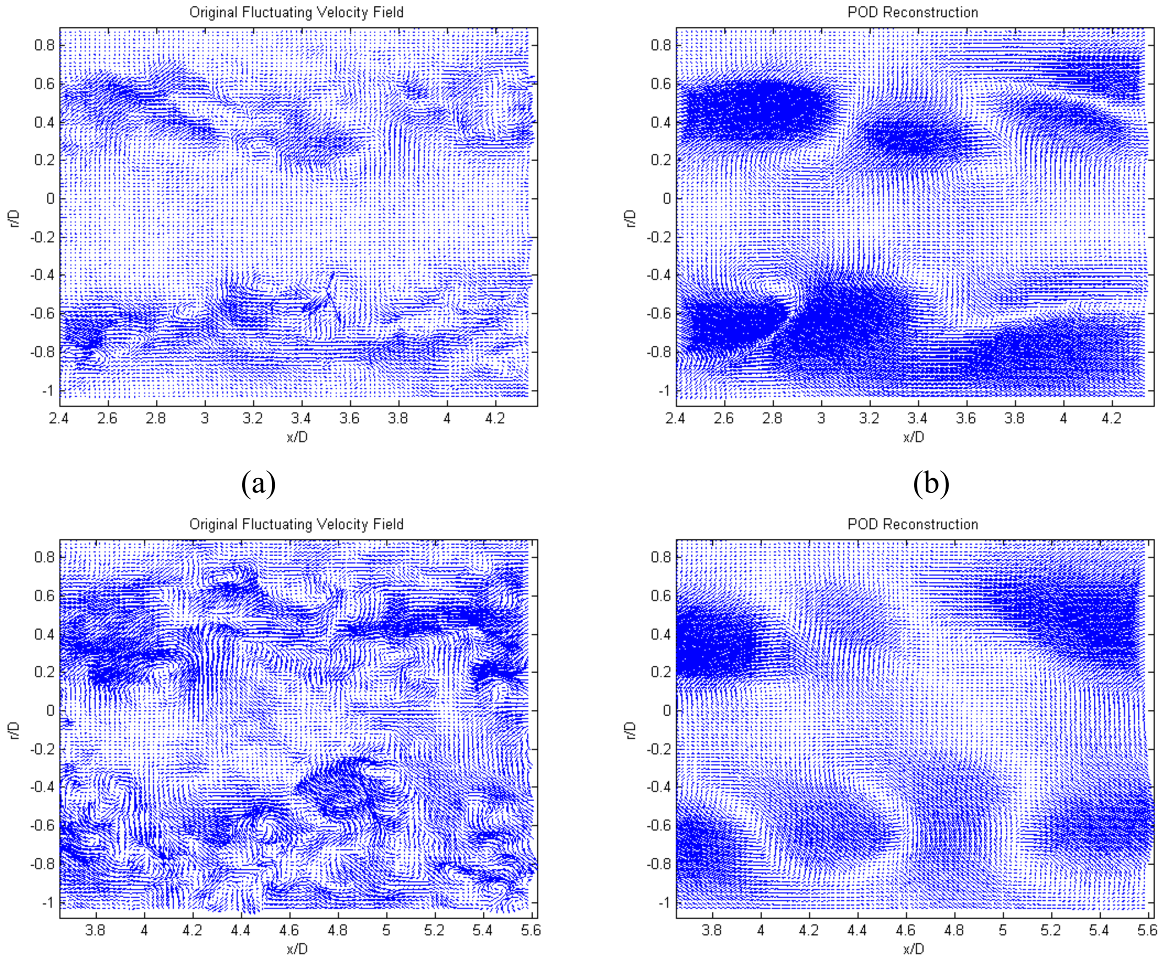

(a) (b)

(c) (d)

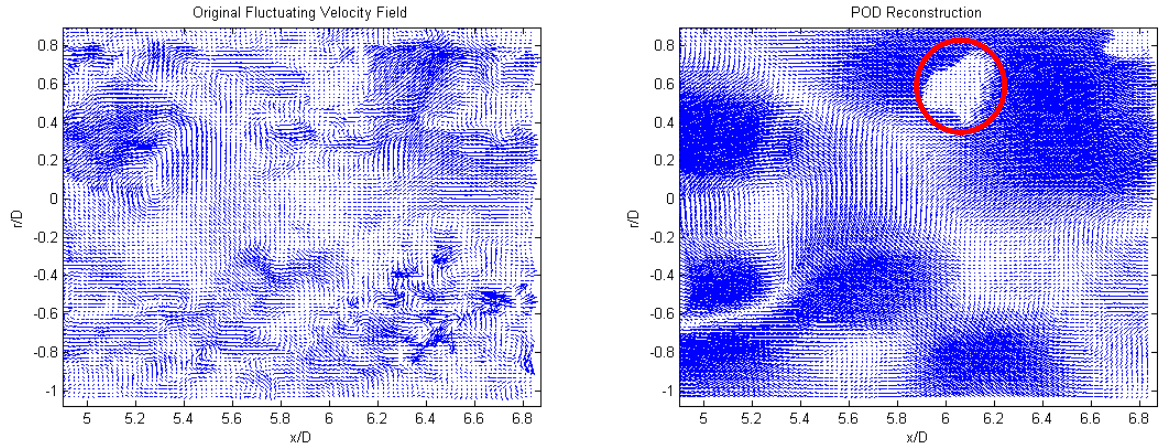

(e) (f)

Figure 17: Stream-wise fluctuating velocity components of the original instantaneous velocity field (left), and the 20 mode reconstruction at three stream-wise locations (right), Controlled jet

E. Cross correlation between Fourier mode filtered pressure and time dependent POD coefficients. The figures below illustrate the cross-correlation between the first 20 expansion coefficients and each of the two strongest energy contributors in terms of the Fourier filtered pressure, mode 0 and mode 1. The Fourier filtered modes are measured at x/D = 6 and the correlations are evaluated across all three measurement planes. The correlation strength grows as we move downstream, or as the distance between PIV measurement location and the azimuthal pressure array is reduced. In the 3 – 4.5D region the correlation magnitudes for the mode 0 and mode 1 are fairly comparable. As we move closer to the azimuthal array, and subsequently the collapse of the potential core region, mode 1 begins to dominate the correlation. It can also be seen that the delay time between the mode 0 and 1 correlations collapse downstream as well. What is noticed is that the coefficients exhibiting the more dominant correlation with the mode 0 component are the higher order modes, as opposed to the mode 1 component, in which the first four time dependent a's have the strongest correlations. In respect to the $a_n(t)$-mode 0 correlation, the physical implications behind what is taking place is not as clear. There is no clear and defined order to which of the 20 modes correlate the most efficiently from one measurement plane to another. The $a_n(t)$-mode 1 correlation on the other hand, appears to appeal more to the first four modes consistently.

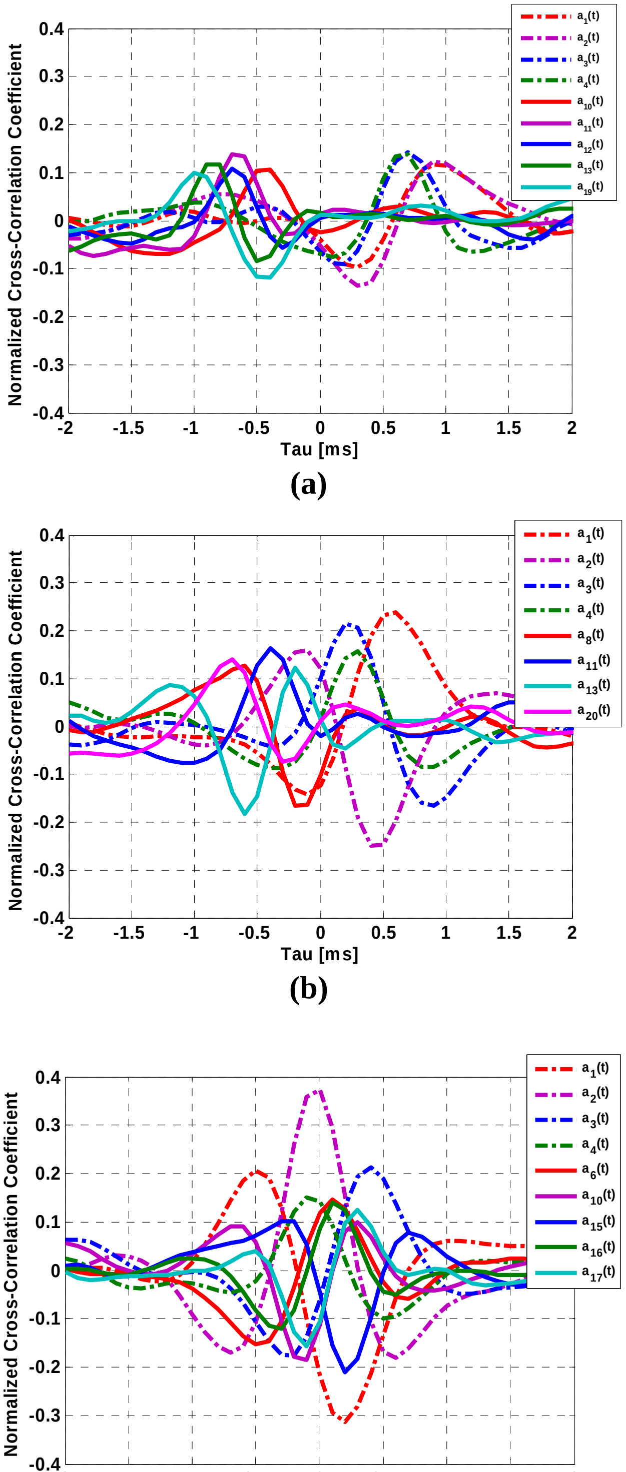

(a)

(b)

(c)

Figure 18: Cross-correlation between first 20 expansion coefficients ($a_n(t)$) and Fourier filtered mode 0 (solid) and mode 1 (dashed), (a) 3 – 4.5 (b) 4 – 5.5 (c) 5 – 6.5

Figure below zeros on the dominant correlation between the near field time dependent expansion coefficients and the far field acoustic region. The same procedure was carried out for the cross correlation between the first 20 time dependent expansion coefficients and each of the 6 far field microphones. All of the cross correlations were on the order of less than 0.05, except for the cross correlation between $\mathbf{a_6(t)}$ and the microphone at 15^0. The time lag is on the same order as the near-field – far-field pressure correlations seen in in our previous papers. What this may indicate is that mode 6 is the mechanism to further explore.

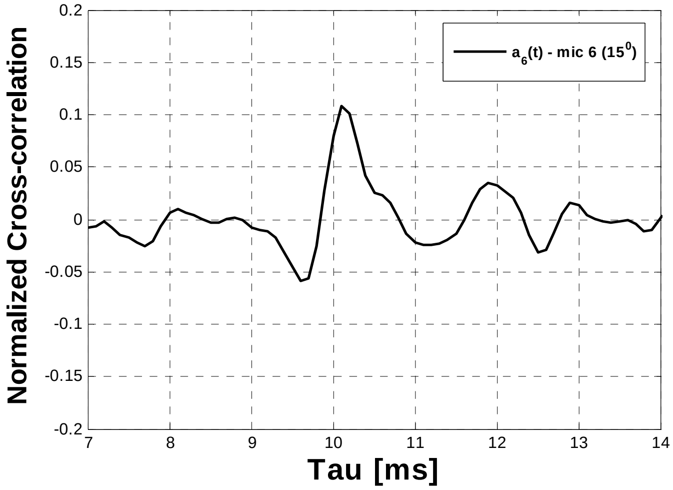

Figure19: Cross correlation between near-field velocity mode 6 for 5 – 6.5D plane and microphone 6.

F. Wavelet Analysis and Near-field Structures

Wavelet decomposition was used on both near- and far-field signals. In the time-frequency domain, the first result pertains to the frequency-dependent convection speed in the near-field, obtained by cross-correlation of the band-passed (wavelet transformed) signals. The results shown here were obtained with the Mexican-hat (continuous) and Daubechies-6(orthogonal) wavelets. The time lags between x/D = 3 and 6 range from 1 to 2ms, with the longer lags (lower convection speed) associated with the lower frequency events.

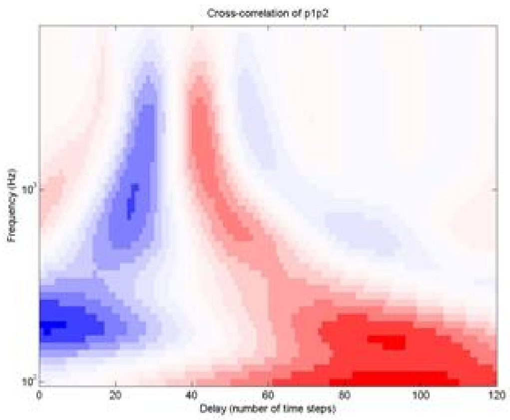

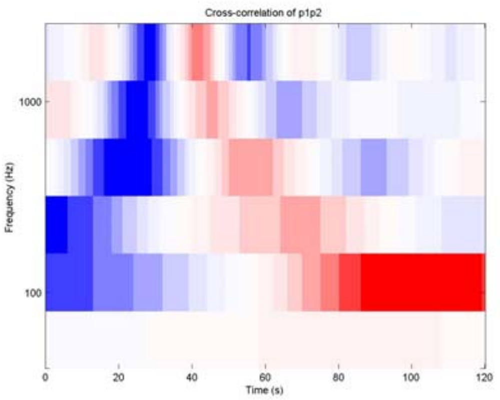

Figure 20: Wavelet-based frequency-dependence of the cross-correlation of mode 0 pressure at x/D = 3 and 6; left: Mexican hat wavelet; right: Daubechies-2 wavelet.

The results for mean convection speeds are similar, but the orthogonality of wavelets was found to be a hindrance in the isolation of individual structures. Using continuous wavelets (Mexican hat and Morlet), some of the events could be recognized from one near-field station to the next, and a decomposition of the mode 0 signals was devised on this basis, and validated (see cross-correlation with far-field for validation). The related flow physics relate to the occurrence, or not, of vortex pairing or breakdown between the two near-field stations.

G. Near-field `matched/residue' decomposition

Based on this decomposition ("matched" traces made of recognized events, "residue" containing the difference between the raw data and the matched events), the signals, spectra and wavelet coefficients are illustrated as follows. The matched signals/spectra are on the left, residue on the right. From this, we see that both the matched events and residue are broad-band signals, intermittent in time and frequency, but the residue captures most of the high-frequency fluctuations. The relevance of this decomposition is illustrated by differences in cross-correlations with the far-field signals, next subsection.

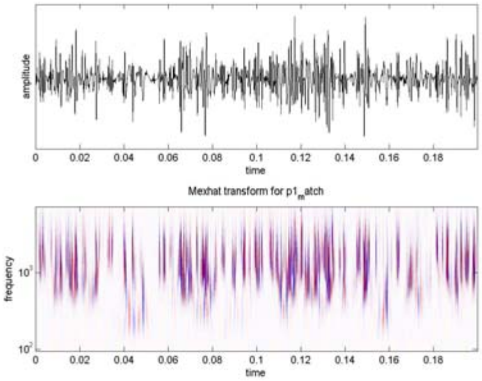

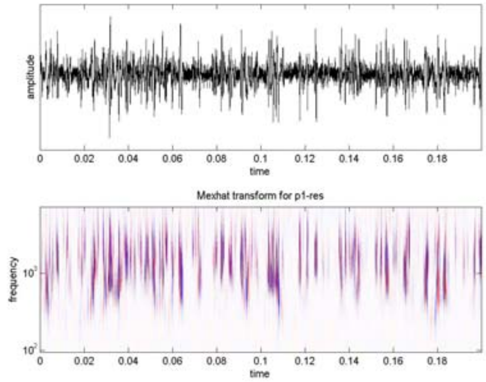

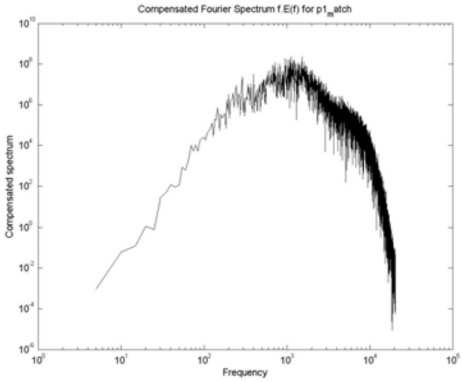

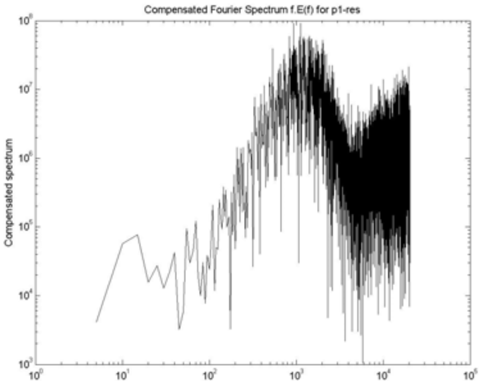

Figure 21: Signals, wavelet coefficients (Mexican hat) (top frames) and compensated Fourier spectra (bottom frames) for the matched events (left) and the residue (right)

H. Frequency-Dependent Cross-Correlations with the Far-Field

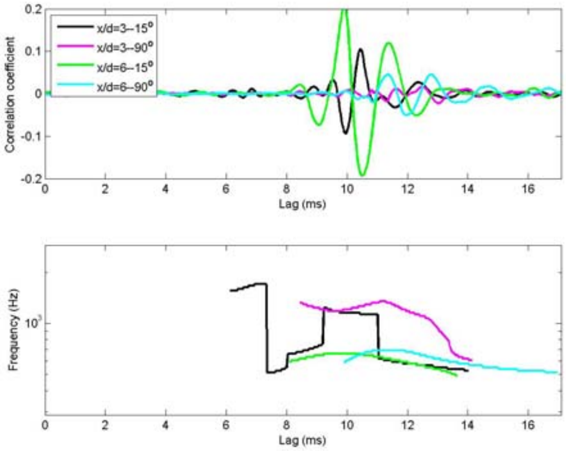

Figure 22: Cross-correlations of four combinations of near-and far-field traces, showing different amplitudes, lags and frequency content.

A comparison of the cross-correlations of either near-field pressure signal (x/D = 3 or 6) with the microphone records at the two extreme locations in the far-field, is shown on Fig 14. The cross-correlations are analyzed for their frequency content, and the strongest ridge of their Morlet wavelet transform was calculated. The transition between dominant frequencies can be abrupt or smooth, with the black and magenta curves as good exemplars. The differences in lags to the 15^o mic (black, green curves) and to the 90^o mic (magenta, cyan curves) are consistent with the effect of sound convection by the jet.

When the same analysis is performed with the matched signals and residue in the near-field, the results are as shown on Fig. 23. The distinction is particularly strong for the x/D = 3 correlations, with changes in both the peak frequency of the cross-correlation and in the shifts in frequency. This points to different populations of sources, and the need to characterize them.

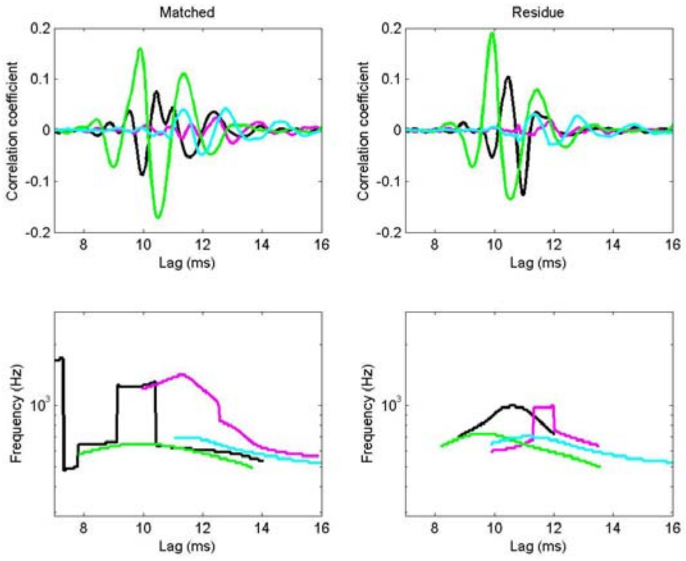

Figure 23: Cross-correlations of matched traces and residue in the near field, with the far-field pressure, otherwise as for Fig. 22.

I. Coherence at the 15-30-45o microphones

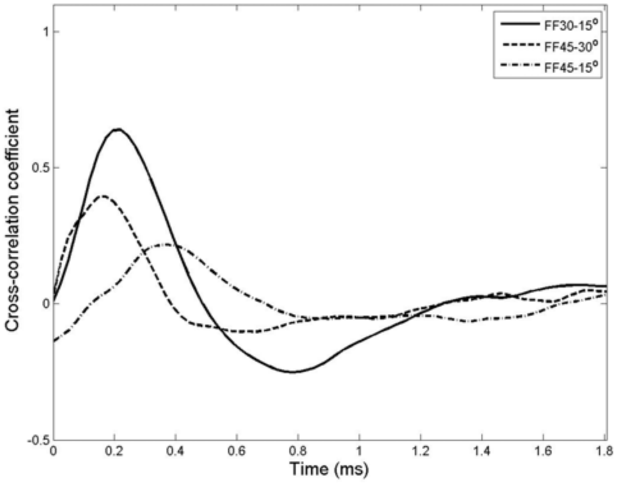

Figure 24: Pairwise cross-correlations between far-field signals from the cone of coherent noise. The smoothness of the curves for single records indicates how similar the signals are.

When we turn to the cross-correlations between far-field traces, coherence for the 15, 30 and 45^o traces is obvious. The cross-correlations for single records (8192 points) are very smooth and reproducible, and the cross-correlation coefficients peak as high as 60% for the $15\text{-}30^o$ pair. This indicates that these microphones hear many of the same things. The signals are then analyzed in the time-frequency domain (wavelets), and yield a clear identification of individual sources.

J. Identification of individual sources from far-field data

The coherence of the far-field noise within 45^o of the jet's axis is highlighted in the time-frequency domain (wavelet transform). The figure shows the wavelet coefficients of two simultaneous traces; each plot consists of patches of loud activity (intense colors) surrounded by less energetic fluctuations; many of the patches are common to the two traces, and therefore they must be associated with individual sources; furthermore, each patch has an oscillatory internal structure (red/blue alternating), which enable us to determine precisely a lag (difference in time of arrival at the far-field microphone) for each source.

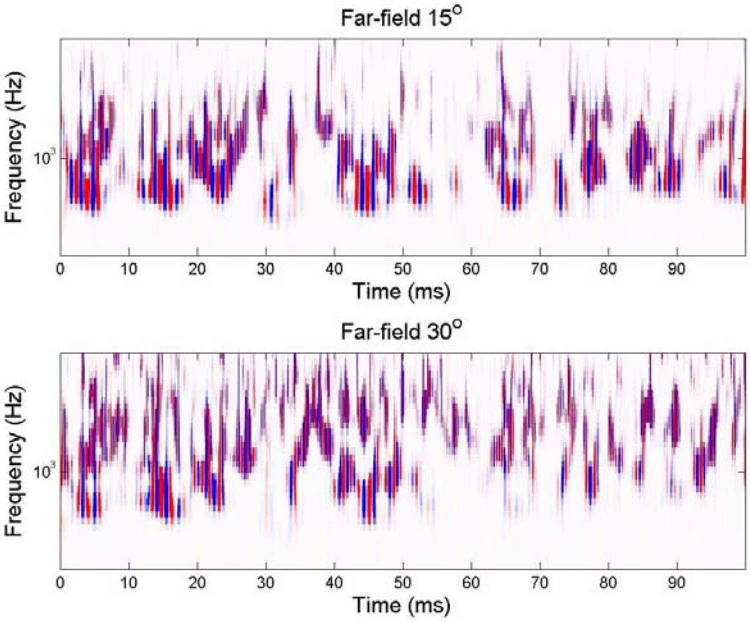

Figure 25: Enhanced wavelet coefficients for two simultaneous pressure traces at 15 and 30^o from the axis; bright colors indicate loud events.

Over the Ma=0.6 database, we built a catalog of over 3000 sources, with lags, magnitude, and frequency. The distribution of lags (Fig. 26, right) shows three general groups of sources: a strong concentration of positive lags will be associated with the region x/D > 6.5, the long slanted line of negative lags with x/D < 6.5, and a less populous group being studied at the time of writing. The probability distribution of positive lags is shown (left). The asterisk denotes the lag (in time steps, at 40960 Hz) corresponding to the peak of cross-correlations between the respective traces, indicating that the sources as identified are consistent with ensemble statistics.

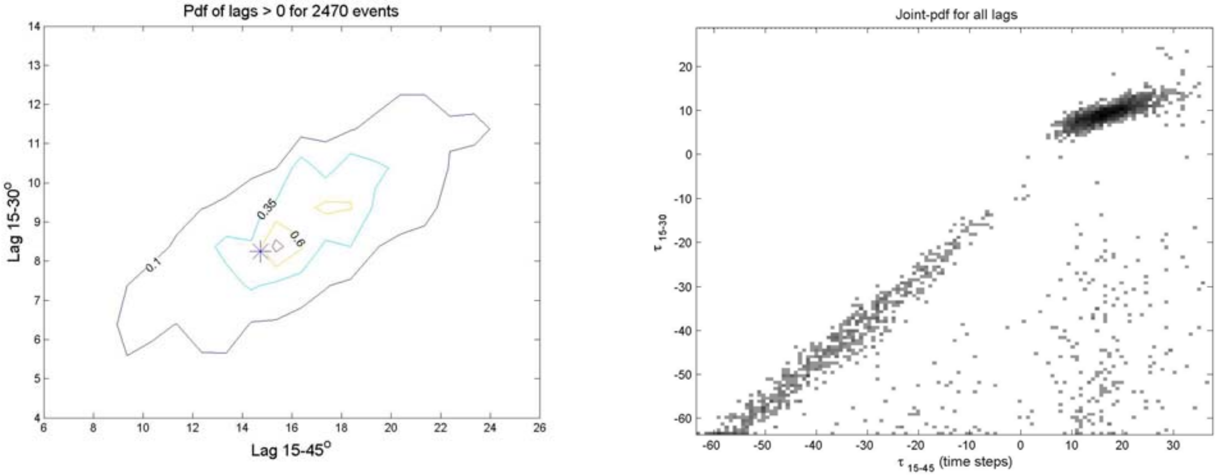

Figure 26: Distribution of positive lags between arrival times of loud events at the 3 microphones closest to the jet's axis.

K. Refraction of Acoustic Paths

It has been known that acoustic paths are deflected by local vorticity (ray tracing). Based on exact inviscid equations and the method of characteristics, acoustic paths from a generic source location to each microphone have been calculated, with propagation times ranging from 9.5 to 11 ms. Thus a table was constructed associating time lags at the microphones with source location. No resolution is possible in the direction normal to the plane of the microphones (spanwise), but some resolution was achieved in the transverse and axial directions. Thus, the catalog of sources detected experimentally was supplemented by an approximate location for each source.

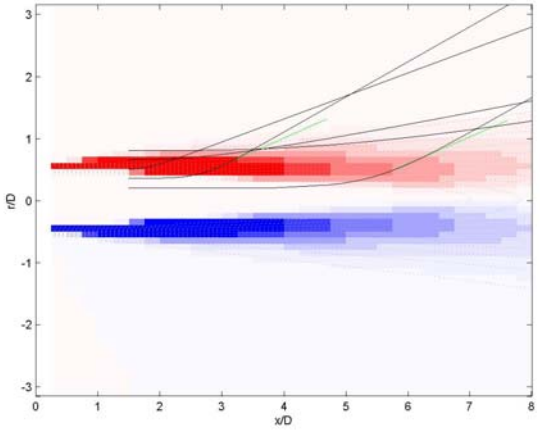

Figure 27: Illustration of the jet's mean vorticity distribution (model) and calculated acoustic paths.

L. Calculated Propagations Times and Lags

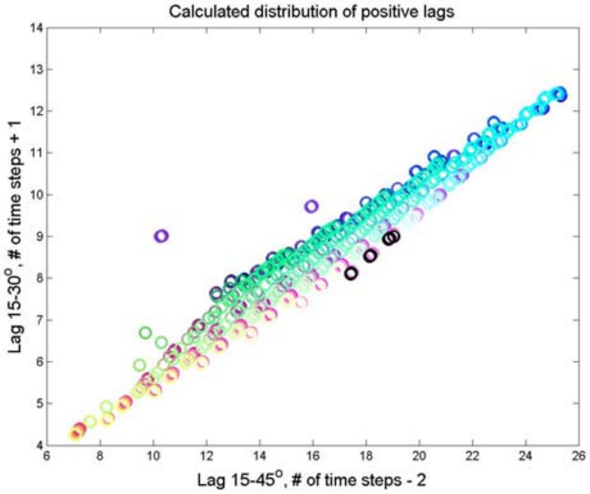

Figure 28: Calculated lags for sources located at increasing axial location (along the long side of the parallelogram, left to right) and across the jet away from the microphones (short side, top to bottom).

The calculated lags, centered around 15 time steps (.4 ms) for 15-45^o and 9 time steps (.22 ms) for 15-30^o, result from the differences between propagation times of the order of 400 time steps. So the 10-15% difference between the measured and calculated lags is if the order of 2% or less of the calculated propagation times, and we consider this to be a remarkable match. The difference in scatter (the experimental pdf is wider than the calculated distribution) has been traced to the effect of coherent vorticity fluctuations (the calculated results shown here are for the mean vorticity field). Fitting a parallelogram on the experimental distribution of lags gives an approximate but simple mapping to 7<x/D<12 and a y-coordinate normalized by the local jet radius.

M. Mapping source properties: shear layer around the potential core

The part of the shear layer on the jet's far side from the microphones cannot be heard by the 15^o microphone, so all data in the region x/D < 7 come from near-side sources. They are the ones with negative lags, and therefore appear to be more numerous (per unit volume of flow) than farther downstream even though they account for only one quarter of the total number of detected sources.

A plot of the joint probability of lags vs. frequency (Fig. 29) shows an abrupt transition. Reading the 15-45o lag as a surrogate of the axial coordinate x/D, we see that a gradual increase in frequency (from bottom-center toward top-right) followed by an abrupt period doubling to a parallel line bottom-left to top center. The transition is occurring near x/D = 4.5, with the most numerous sources being observed at x/D ~ 5.

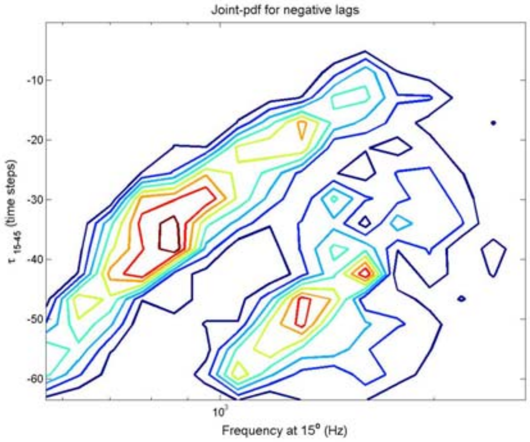

Figure 29: Joint probability distribution of loud events as function of frequency (abscissa) and axial distance (approximate, ordinate) in the region 2.5 < x/D < 6.5

The conditional joint pdf's, grouped by increasing strength of the source (as measured by the magnitude of its wavelet coefficients), clockwise from top left, are shown in Fig. 30. We see the most numerous events at x/D~5 are also the strongest.

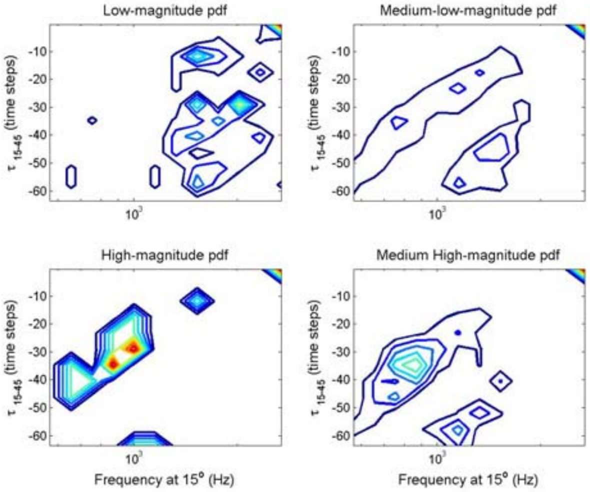

Figure 30: Conditional joint-pdf, sorted in increasing magnitude of event, clockwise from top left; the loudest events occur primarily right after the period-doubling, i.e. around x/D ~ 5.

N. Mapping source properties: mixing region downstream of the potential core

Farther downstream, we have some resolution in the transverse direction. The joint pdf of axial and transverse locations is shown in Fig. 31. Here, the results are consistent with a roughly uniform distribution of sources across the jet, the most numerous sources being located near the plane y/R = 0, and decreasing in numbers away from that plane

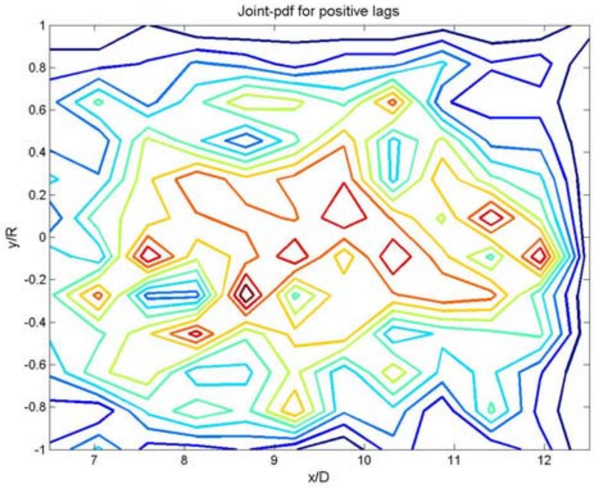

Figure 31: Joint-pdf of sources in the x/D (axial) and y/R (transverse) directions.

The joint pdf for axial location vs. frequency shows a gradual decrease in source frequency as the flow evolves.

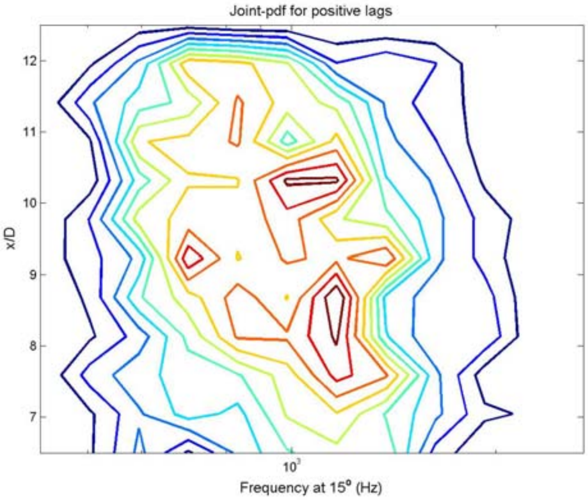

Figure 32: Joint-pdf of sources in the x/D and frequency plane.

Work on mapping the statistics is continuing at the time of writing.

VI. Conclusion

Under the AFOSR funding, we have made excellent progress with the acquisition of state-of-the-art data, with processing of the data by complementary methods including POD and wavelets, and with the modeling of acoustic paths. Significant insight was gained into flow physics in relation to far-field noise, both statistically (through spectra and cross-correlations, and the relation to the velocity POD mode 6) and at the level of individual sources and their characterization. On-going work involves the following ideas

- New data collection to take advantage of what we learned so far
- Focus on minimizing velocity mode 6 as a likely control for far-field noise intensity
- Use the approximate source location from far-field acoustic signals to analyze near-field PIV data
- Find the relation between the statistical content of velocity mode 6 and the loud events identified in the far field.

We have developed unique capabilities in a very promising combination.